

<https://doi.org/10.1038/s43247-025-03141-z>

Anthropogenic fingerprints in global synchronization networks of high aerosol pollution events

Check for updates

Zaibo Zhao^{1,2,9}, Yongwen Zhang^{1,2,9}✉, Dean Chen³, Wenqi Liu^{1,2}, Jun Meng⁴, Jingfang Fan^{5,7}, Xiaosong Chen^{5,6} & Jürgen Kurths^{7,8}

Extreme aerosol pollution events impact climate, air quality, and human health, yet their global synchronization patterns and driving mechanisms remain poorly understood. Here, we construct event synchronization networks to examine both near-field transmission and teleconnection of extreme aerosol pollution events. We find a marked increase in asymmetry within near-field event synchronization networks over recent decades, especially in the Northern Hemisphere, driven by intensified source–sink relationships in high-emission regions. Teleconnection patterns are shaped by Rossby wave activity, making high-aerosol regions increasingly sensitive to atmospheric variability and more susceptible to synchronized extreme events. We find a shift in high teleconnection activity from North America and Europe to Central and East Asia. While major volcanic eruptions can temporarily boost global aerosol synchronization, long-term trends are dominated by anthropogenic forcing. These findings reveal clear anthropogenic fingerprints of extreme aerosol pollution events at a planetary scale, linking regions of intense industrial activity to distant pollution impacts.

Aerosols consist of diverse liquid and solid particles that originate primary from both anthropogenic sources (traffic emissions, industrial processes, residential emissions) and natural sources (dust, sea salt, fungi, volcanic eruptions) and combined sources (biomass burning, secondary aerosols)^{1–3}. They are a significant air pollution, posing serious risks to human health. The World Health Organization estimates that exposure to aerosol pollution contributes to 4.2 million premature deaths annually⁴.

As a crucial component of the Earth's system, aerosols also play a profound role in climate dynamics^{5,6}. They influence global climate patterns, and past events suggest that aerosols may have contributed to significant climatic shifts. A recent study showed that dust aerosols could have a major contribution on the Cretaceous–Paleogene Extinction event⁷. The impact of aerosols on current climate, however, is complex and multifaceted. While some aerosols (i.e. sulfur/sulfate aerosols) contribute to the slowing down of global warming, some species of aerosol (i.e. black carbon) can also produce warming effects^{8–10}. Aerosol forcing has been linked to large-scale hemispheric climate shifts, influencing precipitation patterns and tropical cyclone activity¹¹. Aerosols affect the climate, but the climate, in turn, shapes

the formation, transport, and deposition of aerosols, creating a complex feedback loop. Climate-driven changes in temperature, humidity, and wind patterns can alter the distribution, pathways, and atmospheric lifetime of aerosols^{12–14}. In some cases, aerosols are transported across thousands of kilometers through atmospheric rivers, delivering particles to distant regions and affecting environments far from their origin^{15–17}.

Atmospheric teleconnections further influence aerosol concentrations by shaping large-scale wind and pressure patterns^{18–20}. Studies indicate, for instance, that winter particulate pollution in North China is strongly affected by teleconnections and Rossby wave activity^{21,22}, while tropical climate variations modulate air pollution across East Asia²³. In Europe, reductions in anthropogenic aerosols have impacted weather patterns with consequences for particulate pollution levels as far as North China, underscoring the global reach of teleconnections²⁴. In regions with strongly enhanced anthropogenic emissions, extreme aerosol pollution events are increasingly frequent, amplifying the need to understand aerosol transmission and teleconnection mechanisms. Such understanding is crucial to improve predictive models for long-range aerosol pollution and climate change.

¹Yunnan Key Laboratory of Complex Systems and Brain-Inspired Intelligence, Kunming University of Science and Technology, Kunming, Yunnan, China. ²Faculty of Science, Kunming University of Science and Technology, Kunming, Yunnan, China. ³Institute for Atmospheric and Earth System Research/ Physics, Faculty of Science, University of Helsinki, Helsinki, Finland. ⁴Institute of Atmospheric Physics, Chinese Academy of Sciences, Beijing, China. ⁵School of Systems Science/ Institute of Nonequilibrium Systems, Beijing Normal University, Beijing, China. ⁶Institute for Advanced Study in Physics and School of Physics, Zhejiang University, Hangzhou, China. ⁷Potsdam Institute for Climate Impact Research, Potsdam, Germany. ⁸Department of Physics, Humboldt University, Berlin, Germany. ⁹These authors contributed equally: Zaibo Zhao, Yongwen Zhang. ✉e-mail: zhangyongwen77@gmail.com

To address the complex behavior in the earth system, recent studies have turned to machine learning and data-driven approaches, which excel at identifying hidden patterns in large datasets^{25,26}. Among them, complex network theory has emerged as a particularly promising tool, with applications spanning diverse complex systems over the past two decades^{27–29}. In climate science, network-based approaches have been employed to forecast climate phenomena^{30–33} and to trace pathways of teleconnected elements^{34,35}. Networks, composed of nodes and links that represent regions and their interconnections, provide a robust framework for analyzing intricate relationships through mesoscopic network metrics³⁶. For analyzing point-like time series, such as extreme events, event synchronization (ES) networks have demonstrated particular efficacy in capturing the dynamic behavior of extreme events^{37,38}. These networks have been instrumental in predicting extreme floods³⁹, as well as uncovering synchronized patterns and propagation pathways of extreme rainfall and associated teleconnections^{40,41}.

In this study, we apply the ES network analysis to global aerosol optical depth (AOD) reanalysis data to explore the transmission and teleconnection patterns of extreme aerosol pollution events (EAPEs). By leveraging this approach, we investigate how transmission and teleconnections of EAPEs have evolved over recent decades. Our analysis sheds light on the mechanisms driving these patterns, including the roles of anthropogenic emissions and natural phenomena such as volcanic eruptions. Additionally,

we assess the impact of climate-induced changes in atmospheric circulation, including discuss the activity of Rossby waves, which are critical for maintaining teleconnection systems.

Results

The ES network of AOD

First, we identify EAPEs globally (Fig. 1a) based on the 90th percentile AOD threshold (see Methods). Although the 99th percentile is often used to define extremes, we adopt the 90th percentile to ensure sufficient sample size for robust network statistics. Regions with higher thresholds, as shown in Supplementary Fig. S1a, correspond to major aerosol sources. For example, the Sahara Desert and other arid regions are key sources of primary aerosols, while South and East Asia exhibit high thresholds due to anthropogenic emissions contributing to both primary and secondary aerosols. The spatial distribution of the annual frequency of EAPEs is detailed in the Supplementary Fig. S1b. These events are predominantly frequent in the mid-to-high latitudes of both hemispheres, driven by aerosol formation and accumulation associated with the weather systems in these regions.

To examine shifts during the studied period, we divide the period (1980–2022) into two intervals: Period 1 (1980–2000) and Period 2 (2001–2022). During the latter period, anthropogenic aerosol levels exhibit a significant increase, resulting in a marked rise in the frequency of EAPEs in

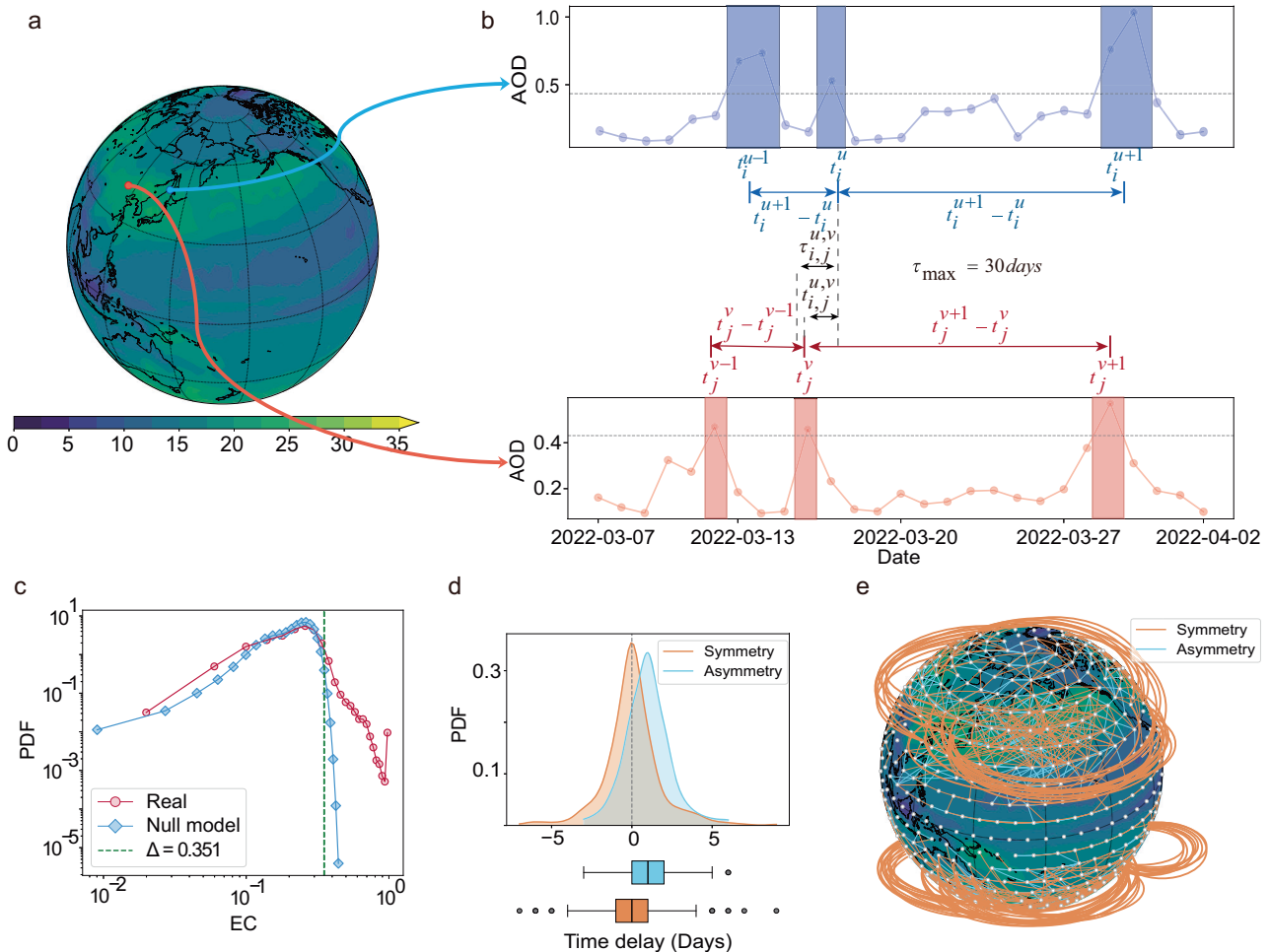


Fig. 1 | Workflow for constructing the ES network of AOD. **a** Spatial distribution of the annual frequency of EAPEs. **b** Example of two AOD time series corresponding to the red grid point (42.5°N, 115°E) and the blue grid point (47.5°N, 140°E) in (a), the red and blue shadows represent the EAPEs in the two time series, respectively, t represents the time at which the event occurs. ES is considered to occur when the timing of EAPEs at the two grids satisfies the synchronization criterion (see

Methods, Eq. (1)), like e_i^u and e_j^v in figure. The gray dashed line indicates the AOD threshold for identifying EAPEs. **c** PDF of EC values for the real data compared with the null model. **d** Examples of PDFs for time delays of synchronization for symmetric and asymmetric synchronization links. **e** Schematic representation of the ES network, illustrating two types of synchronization links.

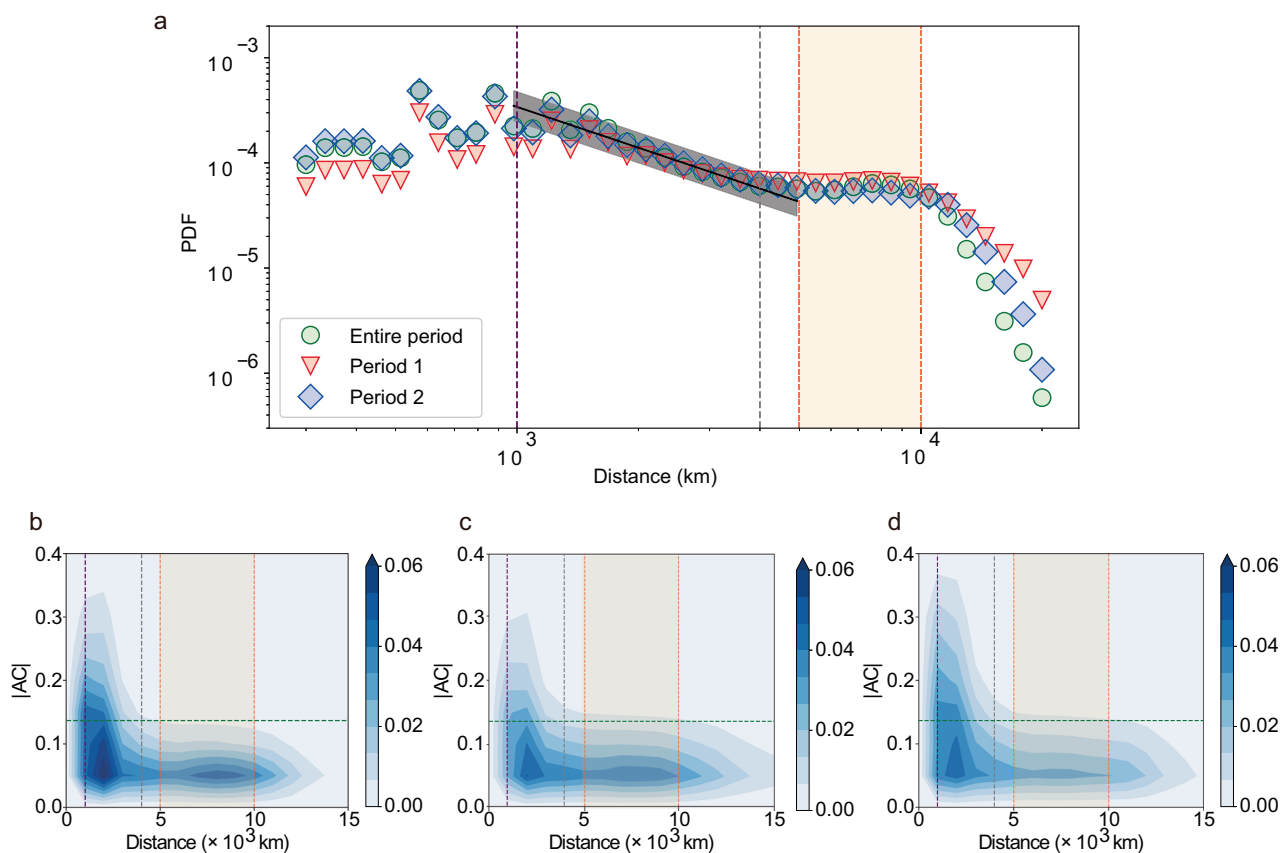


Fig. 2 | Distance-dependent characteristics of links in the ES network. **a** PDF of link distances, with the black fitted line with a slope of -1.67 ± 0.02 . Density plot of absolute asymmetric coefficients ($|AC|$) as a function of link distance for **(b)** the entire period, **(c)** Period 1, and **(d)** Period 2. Pink and gray and orange dashed vertical lines represent 1,000 km and 4,000 km, respectively, the orange shaded area represents the range of 5000–10,000 km. While the green dashed horizontal line marks $|AC| = 0.13$, which is the significance level of 0.05.

regions such as South and East Asia (see Supplementary Figs. S1c,d). In contrast, North America and Europe show a notable decline in the frequency of such events over the past two decades, attributed to industrial relocation and improved environmental governance⁴².

Next, we construct the network from EAPE data based on event synchronization. First, we calculate the event synchronization coefficient (EC) for all grid pairs using Eq. (4) (see Methods). Figure 1b illustrates an example of event synchronization. After determining the occurrence time of EAPEs, we no longer consider the AOD values in the time series but instead focus on whether the timing of extreme events between grid points, we calculate a dynamic delay based on the time intervals between each target event and its neighboring events and by defining a maximum allowable time delay to avoid unreasonable prolonged synchronizations, then compare the minimum of the two delays with the time interval between the target events to determine whether the target event qualifies as a ES (see Methods, Eq. (2)). Furthermore, in order to quantify the degree of event synchronization between two grid points by calculating their rate of ES, we define and calculate the event synchronization coefficient (EC) for all grid pairs using Eq. (4) (see Methods). The probability density functions (PDFs) of EC values for the real data and the null model are presented in Fig. 1c, revealing a fat-tailed distribution for the real EC values. We define the significance threshold Δ as the 99.5th percentile of the null model distribution to identify significant synchronizations as links in the ES network (see Methods). Additionally, the PDF of time delays for synchronization allows us to assess the asymmetry of each link. Figure 1d gives examples of symmetric and asymmetric synchronization links. Asymmetric links indicate a directional flow between locations, often driven by non-equilibrium transmission or diffusion processes, while symmetric links are predominantly influenced by

the large-scale external fields. A schematic representation of the ES network, highlighting these two types of synchronization links, is shown in Fig. 1e. We find that significant network links are primarily zonal rather than meridional. This is demonstrated by the PDFs of the absolute differences in longitude and latitude between connected nodes (Supplementary Fig. S2).

Distance-dependent characteristics of network links

Synchronization links number exhibit distinct characteristics depending on spatial distance, as shown in Fig. 2. The PDF of link distances below 1000 km shows an apparent increasing trend (Fig. 2a). To account for the effect of spatial sampling density, we calculate the fraction of significant links normalized by the number of possible grid-cell pairs in each distance bin (Supplementary Fig. S3). Within 1000 km, this fraction remains close to unity and shows no increasing trend, indicating the high level of synchronization at short distances primarily driven by synoptic-scale weather systems, such as cyclones and anticyclones. Beyond 1000 km, the influence of grid-cell pair counts becomes negligible, and the PDF decreases with distance, following a power-law decay up to approximately 4000 km. In this regime, the influence of synoptic patterns diminishes, and the weakening of synchronization leads to a decrease in the number of synchronization links with increasing distance. Interestingly, at distances greater than 5000 km, synchronization does not continue to decay; instead, it exhibits a stable teleconnection plateau within the 5000–10,000 km range, consistent with the characteristic wavelength of Rossby waves⁴³. Such long-range climate teleconnections have also been reported in studies of extreme rainfall synchronization⁴⁰. In addition, performing the same analysis separately for NH and SH confirms that this stable teleconnection pattern persists robustly in both hemispheres (Supplementary Fig. S4).

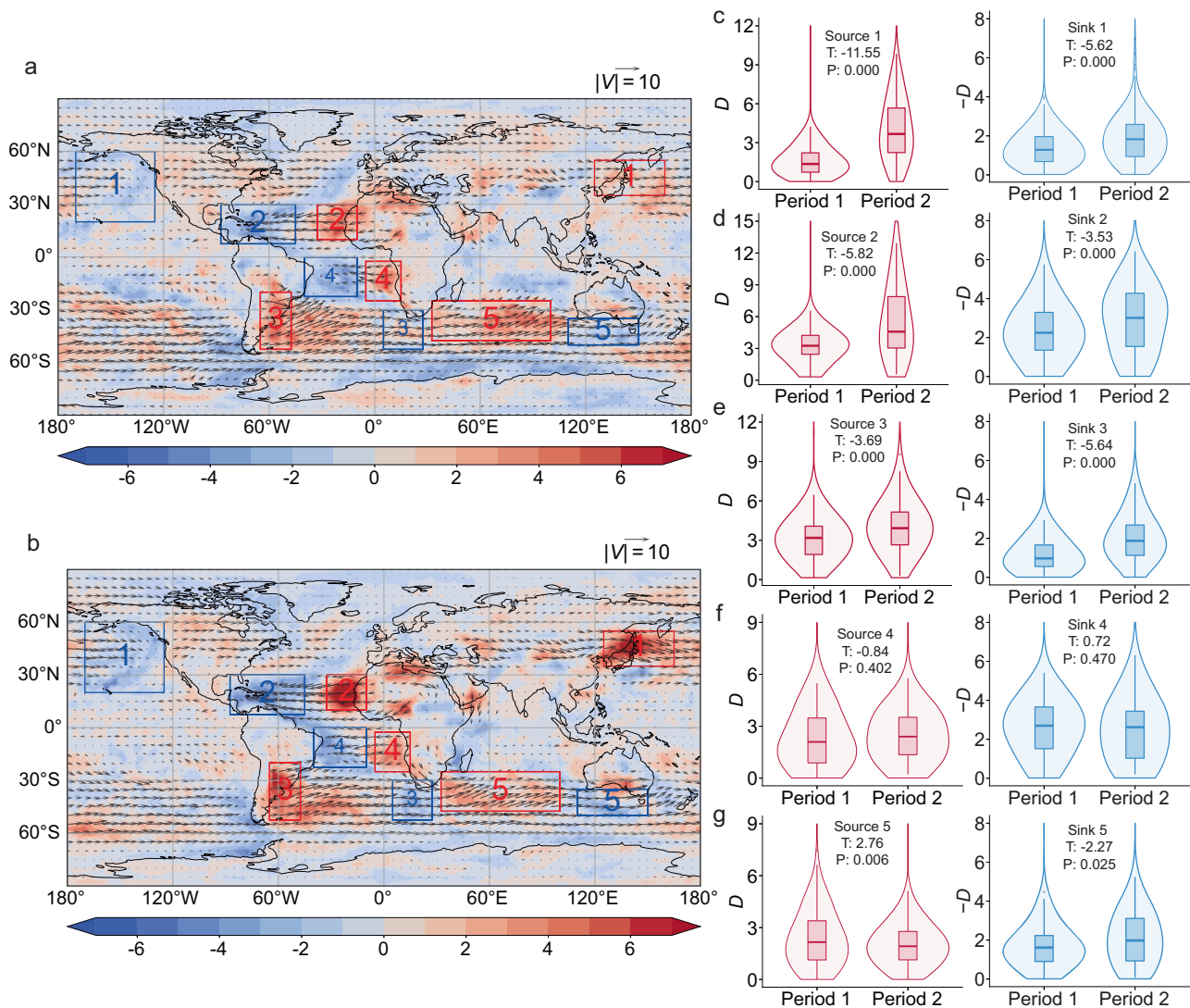


Fig. 3 | Transmission patterns of near-field ES network (link distance < 4000 km) for two periods. a, b Divergence degree (color-coded) and vector degree (represented by arrows) for (a) Period 1 and (b) Period 2. Red and blue rectangles highlight

five key source-sink pairs. **c–g** Violin plots and significance T-tests comparing the divergence degree strength of source-sink pairs between the two periods, with *T* values (*T*) and *P* values (*P*) provided.

The degree of asymmetry in synchronization links is quantified using the asymmetry coefficient (AC) (see Eq. (5) in Methods). Figures 2b–d illustrate the absolute value of AC as a function of link distance across different periods. Strong asymmetry is predominantly observed for links shorter than 4000 km, while links at longer distances exhibit weak asymmetry, falling below the significance threshold (Fig. 2b). This finding supports the interpretation that asymmetric synchronization is driven by non-equilibrium transmission processes, whereas teleconnected synchronization is nearly symmetric. It is noteworthy that short-distance synchronization does not always display asymmetry due to rapid transmission times and the influence of synoptic patterns. Additionally, Fig. 2d reveals that asymmetry is more pronounced in Period 2 compared to Period 1, as shown in Fig. 2c, reflecting potential changes in transmission patterns over time. Meanwhile, compared with Period 1, Period 2 exhibits fewer links within the teleconnection range (5000–10,000 km). Statistical tests confirm that both of these trends are significant (Supplementary Fig. S5).

Transmission and teleconnection network patterns

To further investigate transmission and teleconnection patterns separately, we analyze the near-field ES network with link distances shorter than 4,000 km. The connectivity of each grid to others is quantified

using its weighted degree in the network (see Methods). The weighted degree of a grid is defined as the sum of the EC of all significant links connected to that grid, representing the node’s overall importance or influence within the network. Supplementary Fig. S6 presents the in- and out-weighted degrees of the near-field ES network. Building upon the weighted degree, the in-degree and out-degree further account for the temporal order of synchronized events between two grids. Specifically, the out-degree of a grid considers only those synchronized events in which the extreme event occurs first at that grid point, whereas the in-degree represents the opposite case. The asymmetry in a grid’s connectivity can be assessed through the divergence degree *D*, defined as the difference between the out-degree and in-degree of a grid. Compared to in-degree and out-degree, this metric directly quantifies whether a node is an “influencer” or an “influenced” entity within the network, helping us identify regions that serve as diffusion sources (positive *D*-values) and diffusion sinks (negative *D*-values). Additionally, the vector degree *V* (see Eq. (9) in Methods) provides insights into the directionality of transmission. The supplementary Fig. S7 illustrates the divergence and vector degrees for the entire study period, while Figs. 3a and b show results for Period 1 and Period 2, respectively. Notably, the strength of *D* has increased significantly in Period 2 compared to Period 1, as

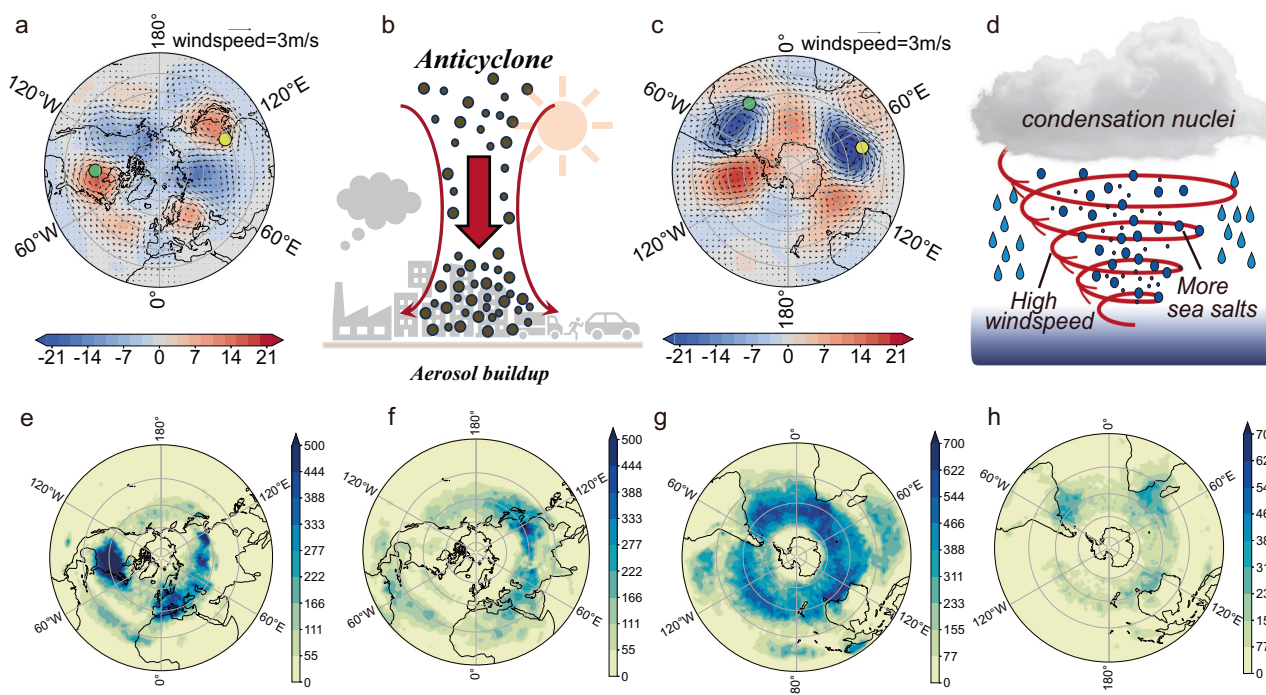


Fig. 4 | Teleconnected ES network patterns (link distance > 5000 km) in NH and SH. **a** Mean 500-hPa geopotential height and wind field anomalies when EAPEs at the yellow point (42.5°N, 115°E) are synchronized with EAPEs at the green point (47.5°N, 90°W). **b** Schematic representation of EAPEs caused by anticyclones in NH. **c** Same as (a), but for the yellow and green points (40°S, 72.5°E) and (40°S, 30°W). **d** Same as (b) but EAPEs caused by low-pressure system and cyclones high windspeed in SH. Spatial distributions of weighted degree in the Northern Hemisphere during (e) Period 1 and (f) Period 2. **g, h** Same as (e, f), but for SH.

highlighted by the PDFs of *D* in the Supplementary Fig. S8a, b, with a particularly prominent increase in the Northern Hemisphere (NH).

We also identify five key source-sink pairs, in Figs. 3a and b. The most significant pair, Source 1 in East Asia and Sink 1 in the Northeast Pacific, exhibits a substantial increase during Period 2. Significance T-tests (Fig. 3c) indicate that the strength of Source 1 and Sink 1 has increased by 157% and 36%, respectively, compared to Period 1. Other notable pairs include Source-Sink 2, with West Africa, which one of the regions that has experienced the most pronounced increase in emissions in recent years due to the impact of human modernization^{44–47}, increasing by 69% and the Gulf of Mexico by 26% (Fig. 3d), and Source-Sink 3, where southern South America has increased by 28% and the west of South Africa by 83% (Fig. 3e). The significant strengthening of these source-sink relationships is primarily driven by the rise in anthropogenic aerosol emissions in developing countries over the past two decades. This increase in emissions has intensified aerosol transmission processes, leading to more pronounced source-sink dynamics within the near-field ES network.

To investigate the mechanisms underlying teleconnected ES, we analyze two typical examples of teleconnections, one from each hemisphere. Figure 4a illustrates the mean 500-hPa geopotential height and wind field anomalies for NH when EAPEs at the yellow grid point are synchronized with those at the green grid point. These points are located within two remote anticyclones. In contrast, when EAPEs at the yellow grid point are not synchronized with those at the green grid point, only the yellow grid point lies within an anticyclone (Supplementary Fig. S9a). Aerosols in land-dominated NH are often strongly linked with anthropogenic emission. Anticyclones and high-pressure systems create stable atmospheric conditions conducive to aerosol accumulation near ground, leading to EAPEs (Fig. 4b).

In Southern Hemisphere (SH), the behavior is similar, but cyclones replace anticyclones. Figure 4c and Supplementary Fig. S9b show that the aerosols, predominantly sea salt from the ocean-dominated SH, are influenced by low-pressure systems. High wind speeds generated by anomalous pressure systems have led to a significant increase in sea salt aerosol

deposition. Concurrently, low-pressure and cyclones systems create conditions that allow these aerosols to remain suspended in the atmosphere rather than settling and dissolving into the ocean surface⁴⁸. The sea salt aerosols then serve as an abundant Cloud Condensation Nuclei (CCN), which partly returns back locally through fog and precipitation (Fig. 4d)⁴⁹. This feedback mechanism explains the frequent occurrence of aerosol pollution events in SH, as shown in Supplementary Figs. S1(b–d). Despite the differences in aerosol types and formation mechanisms between hemispheres, the teleconnected synchronization of EAPEs is primarily driven by the Rossby wave activity. Rossby waves generate several wavenumber-dependent teleconnected synoptic weather systems in mid-latitudes (Supplementary Figs. S9c, d), which synchronously trigger EAPEs.

Since teleconnected links are predominantly symmetric, the teleconnected ES network patterns are represented by the weighted degree of the network for links longer than 5000 km, disregarding directionality. Figures 4e and f illustrate the spatial distributions of weighted degree in NH during Periods 1 and 2, respectively. A comparison reveals a notable shift in regions with relatively high degree values—from North America and Europe in Period 1 to Central and East Asia in Period 2. This trend aligns with changes in the spatial distribution of EAPE frequencies (Supplementary Figs. S1c, d). Regions with more frequent extreme events exhibit stronger synchronization in teleconnections. Notably, since synchronization weight (EC) is normalized by event frequency, this correlation is not trivial. It suggests that regions with high-aerosol concentrations are more sensitive to weather conditions, rendering them more prone to extreme events and teleconnected synchronization.

Supplementary Fig. S10 further shows the teleconnection strength between hotspot regions (North America and East Asia) and other regions as a function of the EAPE frequency in those regions. Across both study periods, regions with higher EAPE frequencies consistently exhibit stronger teleconnections. However, during high-emission periods, teleconnection strength displays a more pronounced sensitivity to EAPE frequency than during low-emission periods (Supplementary Fig. S10g, h). In contrast, under comparable low-emission conditions across different periods, this

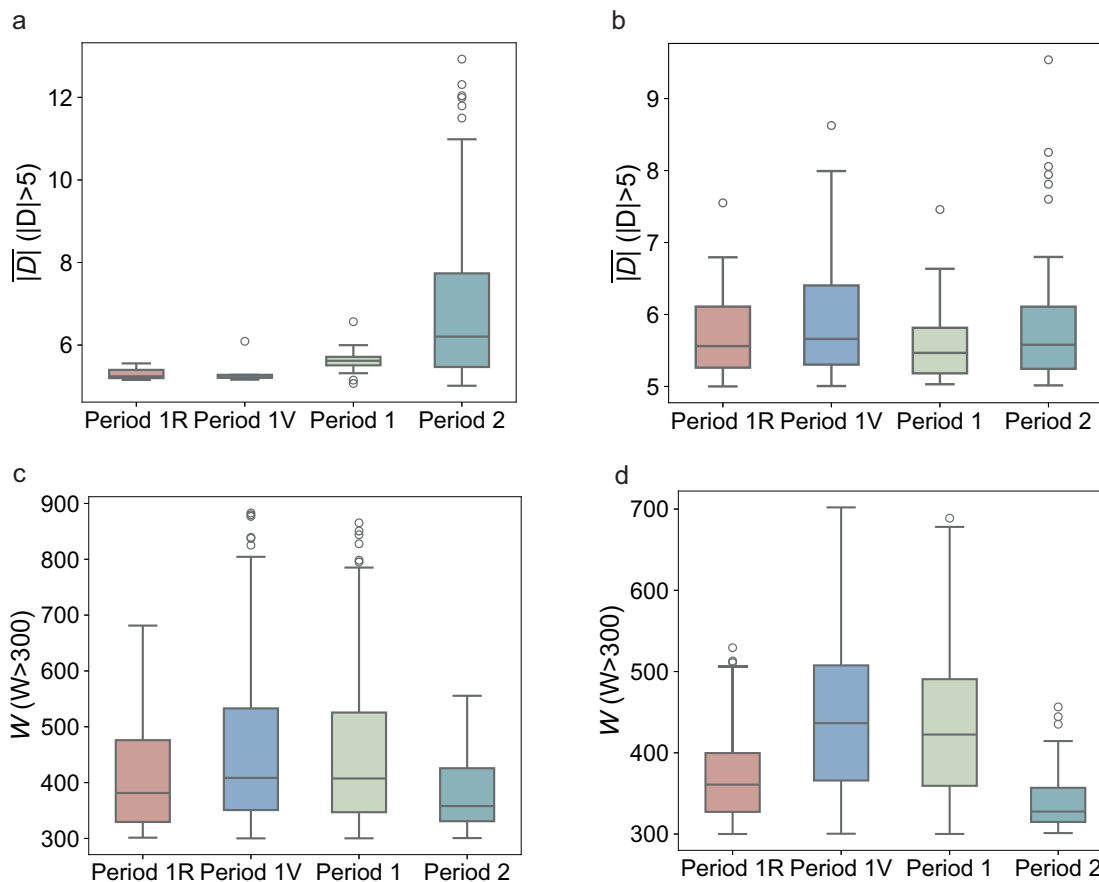


Fig. 5 | Comparison of synchronization patterns during periods dominated by natural factors (volcanic eruptions) and anthropogenic influences. Boxplots showing the grid points ($|D| > 5$) divergence degree strength distribution for the near-field ES network in the (a) Northern Hemisphere and (b) Southern

Hemisphere across different periods. c, d Similar to (a, b), but depicting the grid points ($W > 300$) weighted degree distribution for the teleconnected ES network.

relationship remains similar between the two hotspots, despite climatic variability. These results suggest that the spatial evolution of teleconnection hotspots in the NH is primarily governed by EAPE frequency associated with anthropogenic emissions.

In SH (Figs. 4g and h), teleconnection patterns show a marked weakening in Period 2 compared to Period 1. This weakening is further supported by the PDFs of the weighted degree for the two periods (Supplementary Figs. S11a and S11b). Interestingly, this trend contrasts with the observed strengthening of transmission patterns. While anthropogenic induced aerosol has increased significantly over the past two decades, natural factors such as volcanic eruptions also contribute to global aerosol levels and synchronization events. Furthermore, the weakening of teleconnection patterns may be associated with a decline in Rossby wave activity (amplitude) under climate change, potentially influenced by human activities.

We further examine seasonal influences by repeating the analysis for Period 1 and Period 2 using two seasonal windows-March to August and October to February of the following year (Supplementary Fig. S12). In the NH, transmission and teleconnection patterns are generally stronger from October to February than from March to August. The opposite holds true in the SH. Despite these seasonal contrasts, the overall evolution of network characteristics between Period 1 and Period 2 remains consistent across both seasonal windows.

Impacts of natural and anthropogenic forcing on network patterns

To discern the relative impacts of natural events and anthropogenic factors, we quantitatively isolate the influence of volcanic eruptions within the ES

network. From the annual variation of global AOD, we identify the major natural disruptions as the eruptions of El Chichón in 1982 and Mount Pinatubo in 1991 (Supplementary Fig. S13). The Pinatubo eruption, in particular, caused a more than twofold increase in global AOD, which persisted for several years. Based on this, we define the periods 1982-1984 and 1991-1994 as Period 1V, dominated by volcanic activity. To distinguish volcanic effects, we define Period 1R by excluding Period 1V years from Period 1.

Figures 5 a and b display the divergence degree strength for the near-field ES network in NH and SH during different periods. The divergence degree strength is notably highest in Period 2 in Fig. 5a, indicating the volcanic influence to source-sink dynamics in Period 1V is negligible. The strengthening of the source-sink dynamics appears to be exclusively linked to anthropogenic influences. This trend is particularly pronounced in NH (Fig. 5a) but remains less significant in SH (Fig. 5b) when comparing Period 1R and Period 2. Conversely, the weighted degree for the teleconnected ES network is highest during Period 1V for both hemispheres, as shown in Figures 5c and d. These results suggest that volcanic eruptions significantly increase global aerosol levels, enhancing the sensitivity of various regions to weather patterns and promoting extreme event synchronization⁵⁰.

Figures 5 c and d also reveal that even after excluding volcanic influence, teleconnection synchronization in Period 2 remains weaker than in Period 1R for both hemispheres, though the difference is less pronounced compared to Period 1, which includes volcanic effects. Previous studies suggest that Rossby wave activity is likely to shift under climate change, although substantial uncertainties remain⁵¹. Noteworthy, in the SH, where anthropogenic emissions are relatively low, and the number of EAPEs shows little variation (Supplementary Fig. S14a), volcanic activity almost

entirely dominates the inter-period changes in teleconnections. This dominance is evident both in the magnitude of the weighted degree itself (Fig. 5c) and in its spatial distribution (Supplementary Fig. S14b and c), in stark contrast to the situation in the NH, where human influence plays a much larger role. Some studies have hypothesized increased Rossby wave amplitude due to polar amplification^{52,53}. However, observational data do not corroborate this hypothesis. Instead, some climate models suggested a significant reduction in the Rossby wave amplitude^{51,54,55}. Although the teleconnection synchronization of EAPEs cannot be used as a direct indicator of Rossby wave evolution, it may serve as a complementary, data-driven perspective for understanding changes in Rossby wave activity between Period 1 and Period 2.

Conclusions

Our study provided an investigation into the global synchronization of EAPEs and the underlying mechanisms shaping their spatiotemporal patterns. Through the construction and analysis of the ES networks, in particular by including their asymmetric properties, we identified transmission and teleconnected weather patterns, respectively.

Our findings revealed that the asymmetry in the near-field ES network has significantly strengthened in recent decades, particularly in regions with high anthropogenic aerosol emissions, such as East Asia. This intensification is driven by enhanced source-sink relationships, as evidenced by an increased divergence degree strength. Prominent source-sink pairs, such as East Asia-Northeast Pacific and West Africa-Gulf of Mexico, exhibit a substantial growth in connectivity, largely attributable to rising aerosol production in developing regions. These strengthened source-sink patterns underscore the critical role of human activities in amplifying near-field transmission processes.

Teleconnection patterns are closely linked to Rossby wave activity. Compared with regions of low AOD, regions with high AOD—particularly in the NH are more susceptible to EAPEs induced by Rossby wave-driven local weather systems, which in turn influence teleconnections. We observe a notable shift in regions with relatively high teleconnection degrees, from North America and Europe to Central and East Asia. Over the past two decades, teleconnection patterns in the ES network have weakened, partly due to the volcanic eruptions of El Chichón and Mount Pinatubo, which caused a rapid increase in global aerosol levels and temporarily enhanced teleconnection synchronization. The contribution of Rossby wave dynamics to this weakening under climate change remains uncertain.

This work emphasized the intricate interplay between anthropogenic influences, natural factors, and atmospheric dynamics in shaping global aerosol synchronization. Further research is needed to refine our understanding of Rossby wave dynamics under different climate scenarios and their implications for aerosol-related weather systems and feedback processes.

Method

Data

We use the AOD data from the Modern-Era Retrospective Analysis for Research and Applications, Version 2 (MERRA-2), covering the period from 1980 to 2022⁵⁶. Our analysis focuses on daily-averaged data with a spatial resolution of $2.5^\circ \times 2.5^\circ$ across the globe. Meteorological variables, including geopotential height and wind data, are also sourced from MERRA-2⁵⁷.

Extreme aerosol pollution event

Extreme aerosol height events are identified using a two-step procedure. (a) For each grid cell, days on which aerosol optical depth exceeds the 90th percentile of the full-period distribution are classified as extreme aerosol days. (b) Consecutive extreme aerosol days (≥ 1 day) are then grouped into a single extreme event, with the event onset defined as the first day in the sequence.

Event synchronization

Based on the definition of extreme events, we derive the time series of occurrence times for extreme events, $\{e_i^u\}_{1 \leq u \leq m_i}$ and $\{e_j^v\}_{1 \leq v \leq m_j}$, at grid

points i and j , where n_i and n_j represent the total number of extreme events at grid points i and j , respectively. We assume that an event at grid i can only synchronize with one event at grid j . The synchronization condition is that the absolute time delay, $|t_{ij}^{u,v}| = |e_i^u - e_j^v|$, between events u and v must be less than the minimum of the dynamical delay, $\tau_{ij}^{u,v}$, and a maximum time delay, τ_{max} . Specifically, the dynamical delay is defined as³⁸:

$$\tau_{ij}^{u,v} = \frac{\min(t_{i,i}^{u,u-1}, t_{i,i}^{u+1,u}, t_{j,j}^{v,v-1}, t_{j,j}^{v+1,v})}{2} \quad (1)$$

To avoid unreasonable prolonged synchronizations, we set a maximum time delay of $\tau_{max} = 30$ days. We then define the event synchronization (ES) between a pair of grids (i, j) as the total number of synchronized event pairs:

$$ES_{ij} = \left\| (u, v) : |t_{ij}^{u,v}| < \tau_{ij}^{u,v} \wedge |t_{ij}^{u,v}| < \tau_{max} \right\|, \quad (2)$$

where $|\cdot|$ denotes the absolute value, and $\|\cdot\|$ denotes the cardinality of a set. It satisfies $ES_{ij} = ES_{ji}$.

Simultaneously, we determine the direction of ES based on the sign of the time delay:

$$\begin{aligned} ES_{i \rightarrow j} &= \left\| (u, v) : -\tau_{ij}^{u,v} < t_{ij}^{u,v} \leq 0 \wedge t_{ij}^{u,v} > -\tau_{max} \right\| - \frac{1}{2} \left\| (u, v) : t_{ij}^{u,v} = 0 \right\|, \\ ES_{j \rightarrow i} &= \left\| (u, v) : 0 \leq t_{ij}^{u,v} < \tau_{ij}^{u,v} \wedge t_{ij}^{u,v} < \tau_{max} \right\| - \frac{1}{2} \left\| (u, v) : t_{ij}^{u,v} = 0 \right\|, \end{aligned} \quad (3)$$

where $i \rightarrow j$ indicates that, in the context of ES, extreme events occur at grid i before grid j , and vice versa. Therefore, we have $ES_{ij} = ES_{i \rightarrow j} + ES_{j \rightarrow i}$.

The value of ES is influenced by the number of extreme events at each grid point. To eliminate this effect, we normalize ES by the number of events to obtain the event synchronization coefficient:

$$\begin{aligned} EC_{ij} &= \frac{ES_{ij}}{\sqrt{m_i \times m_j}}, \\ EC_{i \rightarrow j} &= \frac{ES_{i \rightarrow j}}{\sqrt{m_i \times m_j}}, \\ EC_{j \rightarrow i} &= \frac{ES_{j \rightarrow i}}{\sqrt{m_i \times m_j}}. \end{aligned} \quad (4)$$

Here, m_i and m_j denote the number of extreme events at grids i and j , respectively. Thus, the EC is bounded between 0 and 1.

If $EC_{i \rightarrow j} \neq EC_{j \rightarrow i}$, it indicates a directional flow between i and j , reflecting transmission or non-equilibrium diffusion within the system. Conversely, if $EC_{i \rightarrow j} = EC_{j \rightarrow i}$, the synchronization is governed by synoptic or teleconnection patterns. To quantify the asymmetry of synchronization, we define the asymmetry coefficient (AC) as follows:

$$AC_{ij} = \frac{EC_{i \rightarrow j} - EC_{j \rightarrow i}}{EC_{ij}} \quad (5)$$

It is evident that $AC_{ij} = -AC_{ji}$. The value of AC ranges from -1 to 1. A positive AC generally indicates that the flow direction is from i to j , and vice versa.

ES network

The ES network is represented as an $N \times N$ adjacency matrix, \mathbf{G} , with the following elements:

$$G_{ij} = \begin{cases} 1 - \delta_{ij}, & EC_{ij} > \Delta; \\ 0, & EC_{ij} \leq \Delta, \end{cases} \quad (6)$$

where N denotes the total number of grids in the network, and Δ is a significance threshold. The Kronecker delta, δ_{ij} , equals 0 for $i \neq j$ and 1 for $i = j$. If $G_{ij} = 1$, there is a link between grids i and j ; if $G_{ij} = 0$, no link exists between them.

The connectivity of a grid to others is quantified by its weighted degree in the network:

$$W_i = \sum_{j=1}^N G_{ij} EC_{i,j} \cos \theta_j, \quad (7)$$

where $EC_{i,j}$ is the weight of the link and $\cos \theta_j$ accounts for the weight of the area size of grid j , with θ_j representing its latitude.

Given the directional nature of the EC, we define the out- and in-weighted degrees as:

$$W_i^{out} = \sum_{j=1}^N G_{ij} EC_{i \rightarrow j} \cos \theta_j, \quad (8)$$

$$W_i^{in} = \sum_{j=1}^N G_{ij} EC_{j \rightarrow i} \cos \theta_j,$$

The divergence degree, $D_i = W_i^{out} - W_i^{in}$, quantifies the asymmetry between the out- and in-weighted degrees. A positive D_i indicates that grid i influences other grids more than it is influenced by them, while a negative D_i suggests the opposite. A large $|D_i|$ implies that the grid is either a source (positive D_i) or a sink (negative D_i) within the network.

Eq. (8) considers only scalar summation, but synchronization is inherently directional. To capture this, we introduce the vector degrees to describe the net direction of flow for grid i :

$$V_i = \sum_{j=1, AC_{i,j} > 0}^N G_{ij} (EC_{i \rightarrow j} - EC_{j \rightarrow i}) \mathbf{e}_{ij} \cos \theta_j, \quad (9)$$

where the unit vector $\mathbf{e}_{ij} = \frac{1}{l}(\delta\phi, \delta\theta)$, with $l = \sqrt{\delta\phi^2 + \delta\theta^2}$, and $\delta\phi$ and $\delta\theta$ represent the longitude and latitude differences between grids i and j , respectively. In the vector summation process, we consider only one direction of links with stronger synchronization, i.e., those where $AC > 0$, indicating asymmetry synchronization.

Significance testing

The core of the significance test for constructing the ES network lies in selecting an appropriate significance threshold, Δ . Natural time series from Earth systems typically exhibit strong autocorrelation, with power spectral densities of the $1/f$ type and non-Gaussian distributions (e.g., the AOD data shown in Fig. S14). If we base the null hypothesis on Gaussian, uncorrelated noise, we risk underestimating the significance threshold. To mitigate this, we employ the amplitude-adjusted Fourier transform (AAFT) surrogate technique to formulate the null hypothesis^{58,59}. This method, known as phase randomization, preserves the distribution and power spectrum of the original data while removing synchronization and correlation between grid pairs. The steps for determining Δ are as follows: (a) Perform the AAFT algorithm (see Refs. 58,59) on the original AOD time series to generate the surrogate AOD time series for each grid point; (b) Identify EAPEs and compute the EC for the surrogate dataset; (c) Repeat steps (a)-(b) 100 times to generate a distribution of EC values under the null hypothesis; (d) Finally, set the significance threshold Δ as the 99.5th percentile of this null model distribution. This procedure preserves the original power spectrum and distribution of the AOD data while randomizing the phase components, as shown in Fig. S8, allowing for a rigorous test of the statistical significance of the ES network.

Data availability

All Data used in the paper is available from the NASA Goddard Earth Sciences (GES) Data and Information Services Center (DISC) (<https://disc.gsfc.nasa.gov/>). All other data that support the plots within this paper and other findings are provided as a Source Data file and in a Zenodo repository⁴⁷.

Code availability

The analysis codes used in this study have been deposited in Zenodo⁴⁷.

Received: 18 June 2025; Accepted: 15 December 2025;

Published online: 26 December 2025

References

- Prather, K. A., Hatch, C. D. & Grassian, V. H. Analysis of atmospheric aerosols. *Annu. Rev. Anal. Chem.* **1**, 485–514 (2008).
- Prospero, J. et al. The atmospheric aerosol system: an overview. *Rev. Geophys.* **21**, 1607–1629 (1983).
- Seinfeld, J. H. & Pandis, S. N. *Atmospheric Chemistry and Physics: from Air Pollution to Climate Change* (John Wiley & Sons, 2016).
- WHO. *Ambient Air Pollution*. <https://www.who.int/teams/environment-climate-change-and-health/air-quality-and-health/ambient-air-pollution> (2025).
- Pöschl, U. Atmospheric aerosols: composition, transformation, climate and health effects. *Angew. Chem. Int. Ed.* **44**, 7520–7540 (2005).
- Ramanathan, V., Crutzen, P. J., Kiehl, J. & Rosenfeld, D. Aerosols, climate, and the hydrological cycle. *Science* **294**, 2119–2124 (2001).
- Senel, C. B. et al. Chicxulub impact winter sustained by fine silicate dust. *Nat. Geosci.* **16**, 1–8 (2023).
- Li, J. et al. Scattering and absorbing aerosols in the climate system. *Nat. Rev. Earth. Environ.* **3**, 363–379 (2022).
- Storelvmo, T., Leirvik, T., Lohmann, U., Phillips, P. C. & Wild, M. Disentangling greenhouse warming and aerosol cooling to reveal Earth's climate sensitivity. *Nat. Geosci.* **9**, 286–289 (2016).
- Watson-Parris, D. & Smith, C. J. Large uncertainty in future warming due to aerosol forcing. *Nat. Clim. Chang.* **12**, 1111–1113 (2022).
- Cao, J., Zhao, H., Wang, B. & Wu, L. Hemisphere-asymmetric tropical cyclones response to anthropogenic aerosol forcing. *Nat. Commun.* **12**, 6787 (2021).
- Jacob, D. J. & Winner, D. A. Effect of climate change on air quality. *Atmos. Environ.* **43**, 51–63 (2009).
- Carslaw, K. et al. A review of natural aerosol interactions and feedbacks within the earth system. *Atmos. Chem. Phys.* **10**, 1701–1737 (2010).
- Bolan, S. et al. Impacts of climate change on the fate of contaminants through extreme weather events. *Sci. Total Environ.* **909**, 168388 (2024).
- Francis, D. et al. Atmospheric rivers drive exceptional Saharan dust transport towards Europe. *Atmos. Res.* **266**, 105959 (2022).
- Chakraborty, S., Guan, B., Waliser, D. & da Silva, A. Aerosol atmospheric rivers: climatology, event characteristics, and detection algorithm sensitivities. *Atmos. Chem. Phys. Discuss.* **2022**, 1–41 (2022).
- Uno, I. et al. Asian dust transported one full circuit around the globe. *Nat. Geosci.* **2**, 557–560 (2009).
- Feng, J., Liao, H. & Li, J. The impact of monthly variation of the Pacific–North America (PNA) teleconnection pattern on wintertime surface-layer aerosol concentrations in the United States. *Atmos. Chem. Phys.* **16**, 4927–4943 (2016).
- Liu, Y., Liu, J. & Tao, S. Interannual variability of summertime aerosol optical depth over East Asia during 2000–2011: a potential influence from El Niño Southern Oscillation. *Environ. Res. Lett.* **8**, 044034 (2013).

20. Yan, H. et al. Tropical African wildfire aerosols trigger teleconnections over mid-to-high latitudes of Northern Hemisphere in January. *Environ. Res. Lett.* **16**, 034025 (2021).
21. Zhang, Y., Fan, J., Chen, X., Ashkenazy, Y. & Havlin, S. Significant impact of Rossby waves on air pollution detected by network analysis. *Geophys. Res. Lett.* **46**, 12476–12485 (2019).
22. Li, J. et al. Winter particulate pollution severity in North China driven by atmospheric teleconnections. *Nat. Geosci.* **15**, 349–355 (2022).
23. Jung, M.-I., Son, S.-W., Kim, H. & Chen, D. Tropical modulation of East Asia air pollution. *Nat. Commun.* **13**, 5580 (2022).
24. Wang, Z. et al. Reduction in European anthropogenic aerosols and the weather conditions conducive to PM_{2.5} pollution in North China: a potential global teleconnection pathway. *Environ. Res. Lett.* **16**, 104054 (2021).
25. Bergen, K. J., Johnson, P. A., de Hoop, M. V. & Beroza, G. C. Machine learning for data-driven discovery in solid Earth geoscience. *Science* **363**, eaau0323 (2019).
26. Reichstein, M. et al. Deep learning and process understanding for data-driven Earth system science. *Nature* **566**, 195–204 (2019).
27. Barabási, A.-L. & Albert, R. Emergence of scaling in random networks. *Science* **286**, 509–512 (1999).
28. Cohen, R. & Havlin, S. *Complex Networks: Structure, Robustness and Function* (Cambridge University Press, 2010).
29. Newman, M. *Networks* (Oxford university press, 2018).
30. Ludescher, J. et al. Very early warning of next El Niño. *Proc. Natl. Acad. Sci.* **111**, 2064–2066 (2014).
31. Stolbova, V., Surovyatkina, E., Bookhagen, B. & Kurths, J. Tipping elements of the Indian monsoon: Prediction of onset and withdrawal. *Geophys. Res. Lett.* **43**, 3982–3990 (2016).
32. Lu, Z. et al. Early warning of the Indian Ocean Dipole using climate network analysis. *Proc. Natl. Acad. Sci.* **119**, e2109089119 (2022).
33. Fan, J. et al. Network-based approach and climate change benefits for forecasting the amount of Indian monsoon rainfall. *J. Clim.* **35**, 1009–1020 (2022).
34. Zhou, D., Gozolchiani, A., Ashkenazy, Y. & Havlin, S. Teleconnection paths via climate network direct link detection. *Phys. Rev. Lett.* **115**, 268501 (2015).
35. Liu, T. et al. Teleconnections among tipping elements in the Earth system. *Nat. Clim. Chang.* **13**, 67–74 (2023).
36. Donges, J. F., Zou, Y., Marwan, N. & Kurths, J. Complex networks in climate dynamics: Comparing linear and nonlinear network construction methods. *Eur. Phys. J. Spec. Top.* **174**, 157–179 (2009).
37. Arenas, A., Díaz-Guilera, A., Kurths, J., Moreno, Y. & Zhou, C. Synchronization in complex networks. *Phys. Rep.* **469**, 93–153 (2008).
38. Quiroga, R. Q., Kreuz, T. & Grassberger, P. Event synchronization: a simple and fast method to measure synchronicity and time delay patterns. *Phys. Rev. E* **66**, 041904 (2002).
39. Boers, N. et al. Prediction of extreme floods in the eastern Central Andes based on a complex networks approach. *Nat. Commun.* **5**, 5199 (2014).
40. Boers, N. et al. Complex networks reveal global pattern of extreme-rainfall teleconnections. *Nature* **566**, 373–377 (2019).
41. Li, K. et al. Key propagation pathways of extreme precipitation events revealed by climate networks. *npj. Clim. Atmos. Sci.* **7**, 165 (2024).
42. Zhang, Q. et al. Transboundary health impacts of transported global air pollution and international trade. *Nature* **543**, 705–709 (2017).
43. Wang, Y. et al. Dominant imprint of Rossby waves in the climate network. *Phys. Rev. L* **111**, 138501 (2013).
44. Knippertz, P. et al. The possible role of local air pollution in climate change in West Africa. *Nat. Clim. Chang.* **5**, 815–822 (2015).
45. Pante, G. et al. The potential of increasing man-made air pollution to reduce rainfall over southern West Africa. *Atmos. Chem. Phys.* **21**, 35–55 (2021).
46. Haslett, S. L. et al. Remote biomass burning dominates southern West African air pollution during the monsoon. *Atmos. Chem. Phys.* **19**, 15217–15234 (2019).
47. Zhao, Z. Datasets for Anthropogenic fingerprints in global synchronization networks of high aerosol pollution events. *Zenodo*. <https://doi.org/10.5281/zenodo.17892796> (2025).
48. Gong, S. L. A parameterization of sea-salt aerosol source function for sub-and super-micron particles. *Glob. Biogeochem. Cycles* **17**, 1097 (2003).
49. Shi, J. et al. Cyclones enhance the transport of sea salt aerosols to the high atmosphere in the Southern Ocean. *EGUosphere* **2023**, 1–23 (2023).
50. Singh, M. et al. Fingerprint of volcanic forcing on the enso–indian monsoon coupling. *Sci. Adv.* **6**, eaba8164 (2020).
51. Blackport, R. & Screen, J. A. Insignificant effect of Arctic amplification on the amplitude of midlatitude atmospheric waves. *Sci. Adv.* **6**, eaay2880 (2020).
52. Francis, J. A. & Vavrus, S. J. Evidence linking Arctic amplification to extreme weather in mid-latitudes. *Geophys. Res. Lett.* **39**, L06801 (2012).
53. Francis, J. A. & Vavrus, S. J. Evidence for a wavier jet stream in response to rapid arctic warming. *Environ. Res. Lett.* **10**, 014005 (2015).
54. Barnes, E. A. & Screen, J. A. The impact of Arctic warming on the midlatitude jet-stream: Can it? Has it? Will it?. *WIREs Clim. Change* **6**, 277–286 (2015).
55. Francis, J. A., Vavrus, S. J. & Cohen, J. Amplified Arctic warming and mid-latitude weather: new perspectives on emerging connections. *WIREs Clim. Change* **8**, e474 (2017).
56. Global Modeling and Assimilation Office (GMAO). *Merra-2 inst3_2d_gas_nx: 2d, 3-Hourly, Instantaneous, Single-level, Assimilation, Aerosol Optical Depth Analysis v5.12.4* (2015).
57. Global Modeling and Assimilation Office (GMAO). *Merra-2 inst3_3d_asm_np: 3d, 3-Hourly, Instantaneous, Pressure-level, Assimilation, Assimilated Meteorological Fields v5.12.4* (2015).
58. Theiler, J., Eubank, S., Longtin, A., Galdrikian, B. & Farmer, J. D. Testing for nonlinearity in time series: the method of surrogate data. *Phys. D Nonlinear Phenom.* **58**, 77–94 (1992).
59. Lancaster, G., Iatsenko, D., Pidde, A., Ticcinelli, V. & Stefanovska, A. Surrogate data for hypothesis testing of physical systems. *Phys. Rep.* **748**, 1–60 (2018).

Acknowledgements

The authors thank the financial support by the National Key Research and Development Program of China (Grant No. 2023YFE0109000, 2025YFF0517304 and 2025YFF0517203), the National Natural Science Foundation of China (Grant No. 12305044, 12135003, T2525011, 42450183, 12275020, 12205025, 42461144209 and 42575057) and the ClimTip project (ClimTip contribution #35), which has received funding from the European Union’s Horizon Europe research and innovation program under grant agreement no. 101137601. We also thank the data source provided by NASA Goddard Earth Sciences (GES) Data and Information Services Center (DISC) (<https://disc.gsfc.nasa.gov/>).

Author contributions

Z.Z.: Investigation, Visualization, Analysis, Writing Original draft, Reviewing, Editing. Y.Z.: Investigation, Conceptualization, Analysis, Methodology, Writing, Reviewing, Editing, Supervision. D.C.: Methodology, Writing, Reviewing, Editing. W.L.: Methodology, Writing, Reviewing, Editing. J.M.: Methodology, Writing, Reviewing, Editing. J.F.: Methodology, Writing, Reviewing, Editing. X.C.: Methodology, Writing, Reviewing, Editing. J.K.: Methodology, Writing, Reviewing, Editing.

Competing interests

The authors declare no competing interests.

Additional information

Supplementary information The online version contains supplementary material available at <https://doi.org/10.1038/s43247-025-03141-z>.

Correspondence and requests for materials should be addressed to Yongwen Zhang.

Peer review information *Communications Earth and Environment* thanks Matthias Beekmann and the other, anonymous, reviewer(s) for their contribution to the peer review of this work. Primary Handling Editors: Yinon Rudich and Alice Drinkwater. [A peer review file is available.]

Reprints and permissions information is available at <http://www.nature.com/reprints>

Publisher's note Springer Nature remains neutral with regard to jurisdictional claims in published maps and institutional affiliations.

Open Access This article is licensed under a Creative Commons Attribution-NonCommercial-NoDerivatives 4.0 International License, which permits any non-commercial use, sharing, distribution and reproduction in any medium or format, as long as you give appropriate credit to the original author(s) and the source, provide a link to the Creative Commons licence, and indicate if you modified the licensed material. You do not have permission under this licence to share adapted material derived from this article or parts of it. The images or other third party material in this article are included in the article's Creative Commons licence, unless indicated otherwise in a credit line to the material. If material is not included in the article's Creative Commons licence and your intended use is not permitted by statutory regulation or exceeds the permitted use, you will need to obtain permission directly from the copyright holder. To view a copy of this licence, visit <http://creativecommons.org/licenses/by-nc-nd/4.0/>.

© The Author(s) 2025